Research Article

Oxygen Exchange in Dual-Phase La$_{0.65}$Sr$_{0.35}$MnO$_3$−CeO$_2$ Composites for Solar Thermochemical Fuel Production

Alexander H. Bork, Alfonso J. Carrillo, Zachary D. Hood, Bilge Yildiz,* and Jennifer L. M. Rupp*

Cite This: https://dx.doi.org/10.1021/acsami.0c04276

Read Online

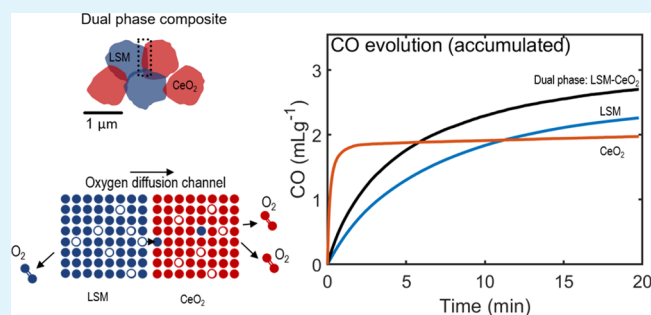ACCESS | Metrics & More | Article Recommendations | SI Supporting Information

ABSTRACT: Increasing the capacity and kinetics of oxygen exchange in solid oxides is important to improve the performance of numerous energy-related materials, especially those for the solar-to-fuel technology. Dual-phase metal oxide composites of La$_{0.65}$Sr$_{0.35}$MnO$_3$−x%CeO$_2$, with x = 0, 5, 10, 20, 50, and 100, have been experimentally investigated for oxygen exchange and CO$_2$ splitting *via* thermochemical redox reactions. The prepared metal oxide powders were tested in a temperature range from 1000 to 1400 °C under isothermal and two-step cycling conditions relevant for solar thermochemical fuel production. We reveal synergetic oxygen exchange of the dual-phase composite La$_{0.65}$Sr$_{0.35}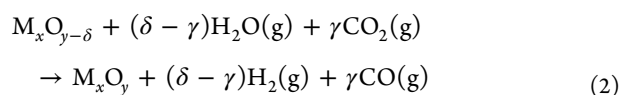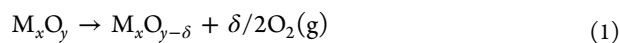MnO_3$−CeO$_2$ compared to its individual components. The enhanced oxygen exchange in the composite has a beneficial effect on the rate of oxygen release and the total CO produced by CO$_2$ splitting, while it has an adverse effect on the maximum rate of CO evolution. *Ex situ* Raman and XRD analyses are used to shed light on the relative oxygen content during thermochemical cycling. Based on the relative oxygen content in both phases, we discuss possible mechanisms that can explain the observed behavior. Overall, the presented findings highlight the beneficial effects of dual-phase composites in enhancing the oxygen exchange capacity of redox materials for renewable fuel production.

KEYWORDS: dual-phase composite, synergy, oxygen exchange, thermochemical CO$_2$ splitting, ceria, lanthanum strontium manganite, solar-to-fuel

1. INTRODUCTION

Two-step solar thermochemical fuel production is an auspicious technology to directly convert solar thermal energy into renewable fuels.[1] The technology has the potential to reduce greenhouse gas emissions, while providing a sustainable supply of energy for transportation and industry. We introduce the principle of a two-step solar thermochemical cycle for a metal oxide with the general structure M$_x$O$_y$ in eqs 1 and 2. In the first step, reduction according to eq 1 is carried out at high temperatures (1200−1500 °C) under an inert atmosphere (pO$_2$ below 10^{-5} atm), in a concentrated solar radiation reactor. In a second low-temperature step at 800−1000 °C, the nonstoichiometric metal oxide is oxidized in the presence of H$_2$O and CO$_2$, producing syngas (H$_2$ and CO), see eq 2.

$$M_xO_y \rightarrow M_xO_{y-\delta} + \delta/2 O_2(g) \tag{1}$$

$$M_xO_{y-\delta} + (\delta - \gamma)H_2O(g) + \gamma CO_2(g)$$
$$\rightarrow M_xO_y + (\delta - \gamma)H_2(g) + \gamma CO(g) \tag{2}$$

Undoped ceria (CeO$_2$) is widely considered as the state-of-the-art material for solar-to-fuel conversion, owing to its fast redox kinetics and phase stability over a wide temperature window.[2−5] A conversion efficiency from carbon monoxide

and water to syngas has been recorded at 5.25%.[6] Indeed, the first experimental demonstration of "solar jet fuel" produced *via* thermochemical splitting of H$_2$O/CO$_2$ with simulated solar radiation was achieved using CeO$_2$.[7] However, the main drawback is the relatively low fuel productivity per unit mass of metal oxide which is limited by its oxygen exchange capacity and high reduction temperature.[8]

Perovskites have gained significant interest as an additional material class besides binary oxides over the past few years for solar-driven thermochemical cycles;[9−17] see also the recent review on perovskites by Kubicek et al.[18] The advantage of perovskites is their large oxygen exchange capacity and the ability of the perovskite structure to accommodate a large number of different cations altering the redox properties. Among the recently studied perovskites, lanthanum manganite is one of the materials that has been studied in most detail for solar-to-fuel conversion.[10,12,17,19−25] For example,

$La_{0.6}Sr_{0.4}MnO_3$ demonstrates a higher oxygen evolution of 0.16 mol kg^{-1} compared to ceria with 0.071 mol kg^{-1} for reduction at 1500 °C and a pO$_2$ of 10^{-3} atm.[26] The main drawback of perovskites is that they have slower oxidation kinetics in comparison to ceria, which is due to a lower thermodynamic drive for oxidation in the presence of water and carbon dioxide.[27] It is possible to enhance the oxidation of the perovskite by using a large excess steam concentration (*i.e.*, a high H_2O/H_2 ratio) or a high carbon dioxide concentration, but this leads to an energy penalty and lower solar thermochemical efficiency.[21,26,27]

Recently, alternative materials with high yields for thermochemical water splitting that require lower steam excess concentrations have been reported. For example, Zhai et al.[28] introduced a new material class of poly-cation oxides $(FeMgCoNi)O_x$, which showed favorable higher H_2 yields compared to ceria for different concentrations of excess steam. They confirmed that ceria is invariant to the H_2O/H_2 ratio because of a high thermodynamic driving force for oxidation in the presence of H_2O. The poly-cation oxide displayed a decline in H_2 production when the steam excess concentration was reduced, but the yield was still higher than the one observed for ceria before the steam excess was reduced to H_2O/H_2 = 100:1 for 5 h of oxidation. In addition, Barcellos et al.[16] have reported a promising new perovskite-type oxide, namely, $BaCe_{0.25}Mn_{0.75}O_{3-\delta}$, which retained a higher H_2 yield compared to ceria and the poly-cation oxides for H_2O/H_2 = 285:1. However, the authors note that 10 h on steam are required to produce a comparatively higher yield of H_2 for all tested conditions. Interestingly, the authors found the presence of an unintentional secondary phase (less than 5%) of ceria in their sample. They scale the H_2 productivity linearly with the amount of the ceria phase present in the sample and conclude that it is responsible for less than 1% of the total H_2 production. The progress made for these metal oxides is encouraging for the discovery of new efficient materials. Yet, the challenge remains to find a material, which is crystallographically stable and shows both high fuel production and fast kinetics.

The scope of this work is to investigate a dual-phase composite of a perovskite, namely, $La_{0.65}Sr_{0.35}MnO_3$, and ceria for the solar-to-fuel conversion technology. The idea is to benefit from the large oxygen exchange capacity of the perovskite and purposefully utilize ceria, both as an active redox material and a catalyst for faster oxygen exchange from the perovskites. Ceria has been investigated broadly as an oxygen exchange promoter and as a catalyst for metal oxides employed as an oxygen exchange material.[29−31] For instance, dual-phase composites such as CeO_2−$CuMnO_2$ displayed improved oxygen release rates for an optimized CeO_2 content when it was tested as an oxygen storage material. With 5 wt % CeO_2, the oxygen storage capacity reached a maximum at ca. 6 wt % for the composite $CuMnO_2$−5 wt %CeO_2 compared to 4.5 wt % for $CuMnO_2$ alone at 600 °C.[29] Here, the authors use the term "oxygen diffusion channel" to describe the observed synergistic phenomena, where CeO_2 enhances the reduction of the bulk $CuMnO_2$ phase. For the same application, Machida et al.[32−34] reported that CeO_2 could act as a "gateway" for synergetic oxygen release for Fe_2O_3, $La_2O_2SO_4$ and $FeMnO_y$. To explore this phenomenon in greater detail, Machida et al.[34] studied the relative oxygen content of CeO_2- and CeO_2-grafted Fe_2O_3 by *in situ* Raman spectroscopy. Under reducing conditions, the oxygen content of the pristine CeO_2 phase

decreases, while the CeO_2 phase in contact with Fe_2O_3 had higher oxygen content. The authors ascribed this observation to lattice oxygen transport from Fe_2O_3 to CeO_2 and hypothesized that this exchange could explain the observed synergy.

Among the composites that have been tested earlier for high temperatures relevant for solar thermochemical fuel production are based on so-called stoichiometric reactions such as the ferrite/hercynite cycle.[35,36] For instance, during reduction, the stoichiometric metal oxide pairs form solid solutions, for example, $Fe_2O_3(s) \rightarrow FeO-Fe_3O_4(s)$.[36] This mechanism is in contrast to the nonstoichiometric metal oxides, such as ceria and the perovskite, where large changes in the oxygen content can be accommodated in the lattice while it remains crystallographically stable, which is desirable from a long-term durability perspective.[18,37]

In this work, we design and test dual-phase nonstoichiometric composites based on the two most prominent materials in the solar-to-fuel field, namely, CeO_2 and strontium-doped lanthanum manganite. The two materials are chosen because they are documented thoroughly in the solar-to-fuel field, which enables a better understanding of the interaction between them. The specific perovskite composition, $La_{0.65}Sr_{0.35}MnO_3$, is chosen because the high strontium content leads to a high oxygen exchange capacity while staying within the bounds of a single-phase perovskite, that is, strontium content higher than 0.47 on the A-site leads to a phase transition.[19] In order to benefit from the high oxygen storage capacity of the perovskite, we choose a phase ratio with a higher content of $La_{0.65}Sr_{0.35}MnO_3$ and add 5, 10, 20, and 50 wt % of CeO_2. The purpose of the chosen ratios is to test whether synergetic exchange occurs in the dual-phase composite and which implications it has for the performance in solar thermochemical cycles. The composites were tested by temperature swing cycling between 1000 and 1400 °C and isothermal cycling between 1200 and 1400 °C, which are typical operating windows for both the perovskite and ceria.[8,19,38] We aim for a material with two distinct phases, mixed on the smallest scale possible to maximize interfacial contact between the two phases to achieve a high oxygen exchange. From the tested compositions, our results reveal for the first time that CeO_2 and $La_{0.65}Sr_{0.35}MnO_3$ display synergistic oxygen release during the reduction step and a higher total fuel production. On the other hand, the rate of oxidation is sluggish compared to the weighted average. Based on the observed synergetic interaction of the components in the dual-phase composite, we perform a detailed structural analysis, that is, XRD and Raman spectroscopy, at different stages of the redox reactions to provide a possible explanation for the existence of synergetic oxygen exchange between the fluorite and perovskite phases.

2. EXPERIMENTAL METHODS

2.1. Materials Preparation. $La_{0.65}Sr_{0.35}MnO_3$−$xCeO_2$ composites were prepared from powders of LSM (Sigma-Aldrich, particle size 0.6−1.2 μm, catalog number 704261) and CeO_2 (Sigma-Aldrich, nanopowder < 50 nm, 99.95% purity) weighed in appropriate amounts (x = 0, 5, 10, 20, 50, and 100 wt %), mixed in deionized water, and sonicated for 15 min. The aqueous solution was then heated to 90 °C under constant magnetic stirring until the water was evaporated. The resulting powder was dried in an oven for 24 h at 80 °C and the powders were subsequently placed in Al_2O_3 crucibles for annealing in a box furnace (Nabertherm) at 1500 °C for 5 h in air with a heating and cooling rate of 5 °C min^{-1}. All samples were

ground to fine powders in an agate mortar and the obtained as-prepared products were referred to as LSM−x%CeO$_2$, where x corresponds to the weight percent of CeO$_2$ of the total weight of the composite. A list of the prepared materials is provided in Table 1.

Table 1. Formula and Label of Prepared Materials[a]

formula	label
La$_{0.65}$Sr$_{0.35}$MnO$_3$	LSM
La$_{0.65}$Sr$_{0.35}$MnO$_3$−5 wt %CeO$_2$	LSM−5%CeO$_2$
La$_{0.65}$Sr$_{0.35}$MnO$_3$−10 wt %CeO$_2$	LSM−10%CeO$_2$
La$_{0.65}$Sr$_{0.35}$MnO$_3$−20 wt %CeO$_2$	LSM−20%CeO$_2$
La$_{0.65}$Sr$_{0.35}$MnO$_3$−50 wt %CeO$_2$	LSM−50%CeO$_2$
CeO$_2$	CeO$_2$

[a]All materials were mixed and sonicated in deionized water and subsequently dried for 24 h prior to annealing at 1500 °C for 5 h in air with a heating and cooling rate of 5 °C min^{-1}.

Samples used for the *ex situ* structural analysis were placed in an alumina tube and exposed to an identical temperature and atmosphere conditions as in the thermochemical cycling experiments and quenched with a cooling rate of 150 °C min^{-1} inside an IR Furnace, ULVAC VHT-E44 controlled with an S-type thermocouple.

2.2. Materials Physicochemical Characterization. Structures of all samples were collected by X-ray powder diffraction (XRD) on a PANalytical X'Pert PRO MPD diffractometer. Cu Kα radiation (Ge monochromator) produced with an extraction voltage of 45 kV at 30 mA current was used to scan the samples in a Bragg−Brentano geometry in the range of 20° < 2θ < 90° with a spinning speed of 60 rpm, a step width of 0.008°, and irradiation time of 1 s. Unit cell parameters were calculated by full profile Rietveld refinement with PANalytical X'Pert Highscore Plus software. Scanning electron microscopy (SEM) was completed on a Zeiss Merlin high-resolution SEM with an acceleration voltage of 5−10 kV. Energy-dispersive X-ray spectroscopy (EDS) elemental mapping was completed with an acceleration voltage of 15.0 kV. Raman spectra were acquired on a confocal WITec Alpha300 R Raman microscope instrument (WITec Germany) equipped with a 457 nm laser, using the 100-fold magnification objective and laser power of 1 mW, together with a spectral resolution of 0.54 cm^{-1}. The collected spectra consisted of six accumulations with an integration time of 30 s.

2.3. Thermochemical Cycling. The experimental setup to determine the oxygen evolution and CO$_2$ splitting properties of the dual-composite is described elsewhere, ref 15, and a short description is included in Supporting Information S1 for completeness. A temperature program was designed to assess the CO$_2$ splitting performance of each material at different oxidation temperatures with a cycling program consisting of eight reduction/oxidation cycles. The first three cycles evaluated the CO$_2$ splitting behavior at three isothermal temperatures (1200, 1300, and 1400 °C) and cycles four to seven were performed under a temperature-swing scheme. Finally, the material was subjected to one more isothermal cycle at 1400 °C. Reduction was carried out at 1400 °C for 20 min, after which the temperature was cooled down to the desired value for the CO$_2$ splitting. All reactions were performed at atmospheric pressure and the oxygen partial pressure was pO$_2$ = 5 × 10^{-5} atm (50 ppm) during reduction in a flow of 300 mL min^{-1} Ar, as measured by our gas analyzer.

After reaching the programmed temperatures (1000, 1100, 1200, and 1300 °C), CO$_2$ was injected at a concentration of pCO$_2$ = 0.5 atm for 20 min. All heating ramps were set to 50 °C min^{-1}. Cooling ramps were set to 50 °C min^{-1} but were slower in practice because of thermal inertia of the electric furnace, for example, cooling from 1400 to 1000 °C took 18 min, instead of the set time of 8 min. For *ex situ* structural analysis of the thermochemical cycles, rapid heating and cooling rates were carried out with an infrared furnace with heating rates set at 150 °C min^{-1}. The samples were placed in an alumina tube and the gas atmosphere was controlled by Voegtlin mass flow controllers with identical flows as in the thermochemical cycling experiments. A cooling ramp was set to match the 18 min for the cooling before exposure to CO$_2$.

3. RESULTS

3.1. Structural Characterization of LSM−x%CeO$_2$ Dual-Phase Composites. All prepared dual-phase composite materials are summarized in Table 1. The composites are based on commercially available CeO$_2$ and La$_{0.35}$Sr$_{0.65}$MnO$_3$, which are acquired in the available particle size for ceria (average particle size < 50 nm) and LSM (average particle size 0.6−1.2 μm) to enable mixing on the smallest scale possible. The powders were mixed in deionized water, sonicated for 15 min, and annealed at 1500 °C for 5 h with heating and cooling rates of 5 °C min^{-1}. Here, the high temperature during preparation was chosen to induce possible structural changes before thermochemical cycling experiments.

To investigate the microstructure of the as-prepared perovskite−fluorite composites, we turn to SEM in Figure 1. The constituent end-member materials, that is, LSM and CeO$_2$, display signs of sintering, in Figure 1a,f. For example, sintering is evident by grain growth and neck formation between neighboring grains of the perovskite and fluorite phases. The composites, as shown in Figure 1b−e, display finer
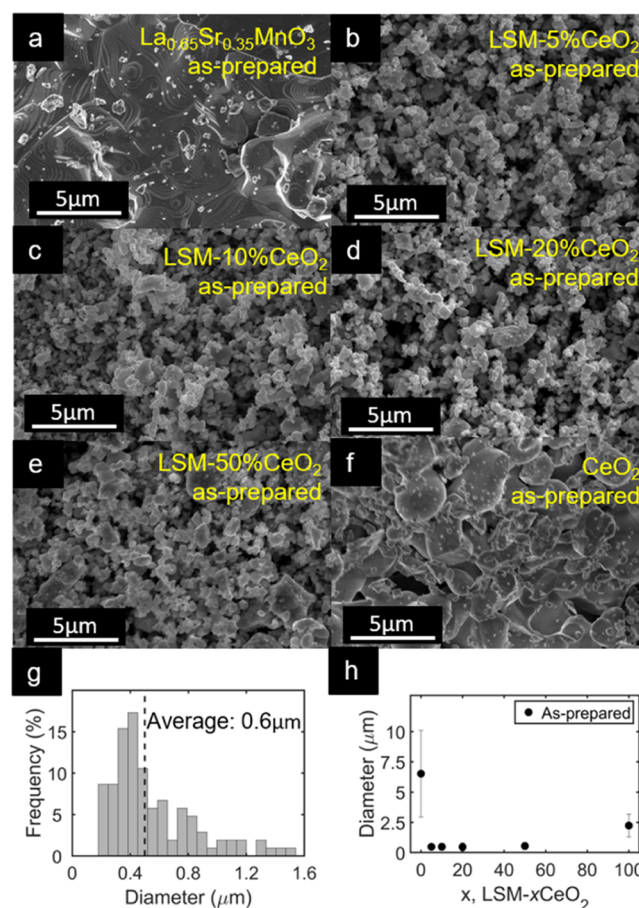

Figure 1. SEM images of as-prepared La$_{0.65}$Sr$_{0.35}$MnO$_3$−xCeO$_2$ powders. (a−f) Corresponds to x = 0, 5, 10, 20, 50, and 100%, respectively, where x is the weight percentage of CeO$_2$ in the dual-phase composite. (g) Grain diameter distribution of LSM−50%CeO$_2$ of the as-prepared composite. (h) Average grain diameter for as-prepared La$_{0.65}$Sr$_{0.35}$MnO$_3$−xCeO$_2$ composites.

grains, where the two phases are in contact, with some observable neck formation between the neighboring grains. The grain size distribution, determined by the SEM image analysis, is shown as an example for x = 50 wt % in Figure 1g. The composite LSM−50%CeO$_2$ has a grain size average of 0.6 ± 0.2 μm Figure 1g, which is smaller than either LSM or CeO$_2$, with a grain size of 6.5 ± 3.6 and 2.2 ± 0.9 μm, respectively, as shown in Figure 1h. Decreased grain growth suggests that diffusion and sintering was impeded for the dual-phase composites. A similar observation of decreased grain growth was made for a composite of a well-mixed dual-phase composite of Gd-doped ceria and LSM obtained by ball milling and sintering.[39] The finer structure, that is, grain size and porosity, of the composite materials could suggest enhanced kinetics may be observed for these materials because of a higher specific surface area. However, it is worth noting that for most relevant conditions for solar thermochemical fuel production, that is, temperatures above 1000 °C, the thermodynamics of the oxygen exchange reaction overrules the effects of grain size and porosity.[19,27]

X-ray powder diffraction patterns of as-prepared La$_{0.65}$Sr$_{0.35}$MnO$_3$−x%CeO$_2$ (where x corresponds to weight percent, x = 0 to 100%) composites are presented in Figure 2.
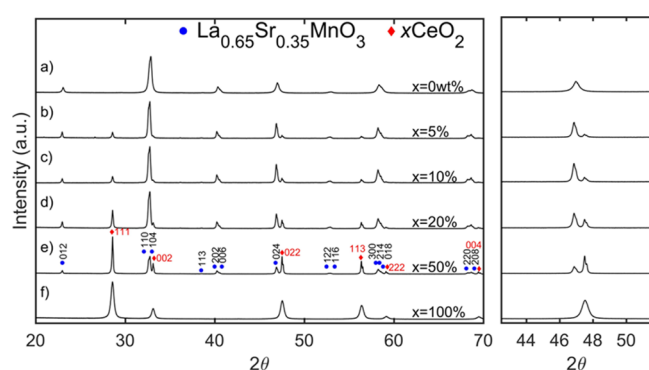

Figure 2. Powder X-ray diffraction patterns of the as-prepared La$_{0.65}$Sr$_{0.35}$MnO$_3$−x%CeO$_2$ composites with x = 0, 5, 10, 20, 50, and 100 wt % in figures (a−f), respectively. In the XRD pattern of the LSM−50%CeO$_2$, (e) all peaks are indexed by the constituent phases La$_{0.65}$Sr$_{0.35}$MnO$_3$ and CeO$_2$ with the rhombohedral structure ($R\bar{3}c$ space group) for the perovskite and the cubic structure ($Fm\bar{3}m$ space group) for ceria. Subfigure on the right is a zoom of the two peaks at a 2θ range of 44−50° corresponding to the (024) plane of the perovskite and (022) plane of the ceria structure.

The pattern of the commercial La$_{0.65}$Sr$_{0.35}$MnO$_3$ (LSM) and CeO$_2$ powders can be indexed to a pure rhombohedral structure and the cubic fluorite structure, respectively, in agreement with the literature.[37,40] For the powder composites of La$_{0.65}$Sr$_{0.35}$MnO$_3$−x%CeO$_2$, all peaks may be identified according to their constituents La$_{0.65}$Sr$_{0.35}$MnO$_3$ and CeO$_2$ and no impurity phases are detectable. An exemplified Rietveld refinement fit of the LSM−50%CeO$_2$ is shown in Supporting Information Figure S1, confirming the phase composition of La$_{0.65}$Sr$_{0.35}$MnO$_3$ and CeO$_2$.

Raman spectroscopy reveals insights on the vibrational bonds of the composite and oxygen nonstochiometry.[41] In Figure 3, pure ceria is compared to the LSM−50%CeO$_2$ sample: the characteristic symmetric stretching mode observed at 464 cm^{-1}, for the as-prepared CeO$_2$ sample is attributed to the F$_{2g}$ Raman mode which can be viewed as a breathing mode of O atoms around the cerium cation,[4,42−45] see also the recent
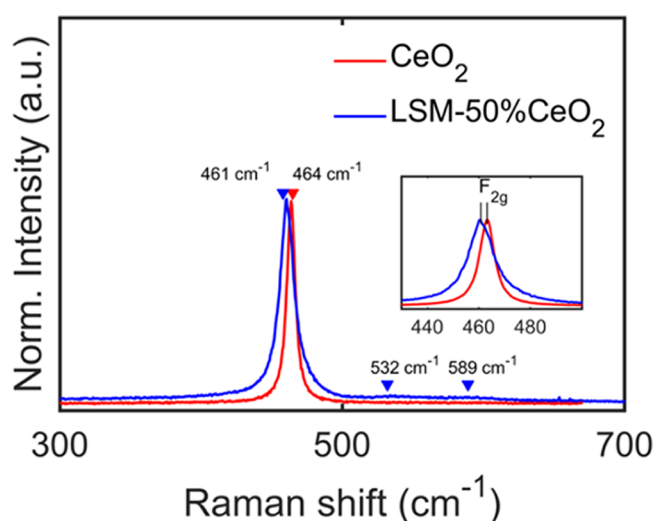

Figure 3. Raman spectra acquired with a 457 nm laser and laser power of 1 mW of as-prepared powders annealed at 1500 °C for LSM−50%CeO$_2$ and CeO$_2$. Inset shows the characteristic F$_{2g}$ peak of CeO$_2$ in the dual-phase composite and pure CeO$_2$.

review for ceria near-order spectroscopy details.[46] In the spectra acquired of the composite, x = 50 wt %, the broad Raman bands typically observed at 400−800 cm^{-1} for the LSM perovskite are not distinguishable because of a strong signal of a distinct peak at 461 cm^{-1}. This latter peak is ascribed to the F$_{2g}$ peak of CeO$_2$ shifted to a lower wavenumber accompanied by peak broadening with a change in full width half maximum (fwhm) from 7 to 13 cm^{-1}. Both Mn and La are present in the perovskite, and small doping concentrations of Mn or La in CeO$_2$ can result in a peak shift to lower wavenumbers and peak broadening,[44,47] which is ascribed to lattice expansion. However, the two weak shoulders at the higher wavenumbers (532 and 589 cm^{-1}) are commonly observed only for lanthanum-doped ceria[44] and +3 dopants substituting Ce, which introduces defect vibrational bands.[48] According to a systematic Raman study of rare earth (La, Pr, Nd, Eu, Gd, and Tb) doping in ceria by McBride et al.,[44] and a recent review by Schmitt et al.,[46] La-doping results in a gradual shift of the F$_{2g}$ peak to lower wavenumbers and an increase in the relative height of the shoulder with respect to the F$_{2g}$ peak. Based on the observed shift of Δ = 2.4 cm^{-1} for the F$_{2g}$ peak and the available literature, we estimate that ceria in the composite has a small doping concentration of La between 1 and 5 atomic % after processing (via sintering of the ceramic).

In summary, the structural analysis, XRD, SEM, and Raman spectroscopy confirm a dual-phase composite that remains in two distinct phases, which are intermixed at the micron scale. Indications of a low doping concentration of La in the ceria phase can be observed, that is lower than 5 atomic % based on a conservative estimate by the Raman spectroscopic analysis. We now turn to thermochemical cycling experiments to test how the dual-phase composites perform under conditions relevant for solar-to-fuel conversion.

3.2. Oxygen Release and CO$_2$ Splitting of LSM−x%CeO$_2$ Dual-Phase Composites. Solar thermochemical cycling properties of the composite LSM−x%CeO$_2$ is assessed by their O$_2$ evolution and CO$_2$ splitting 1000−1400 °C, as shown in Figure 4. The reaction times for reduction and oxidation of 20 min are chosen to match earlier reports and provide an assessment within a window of efficient operation
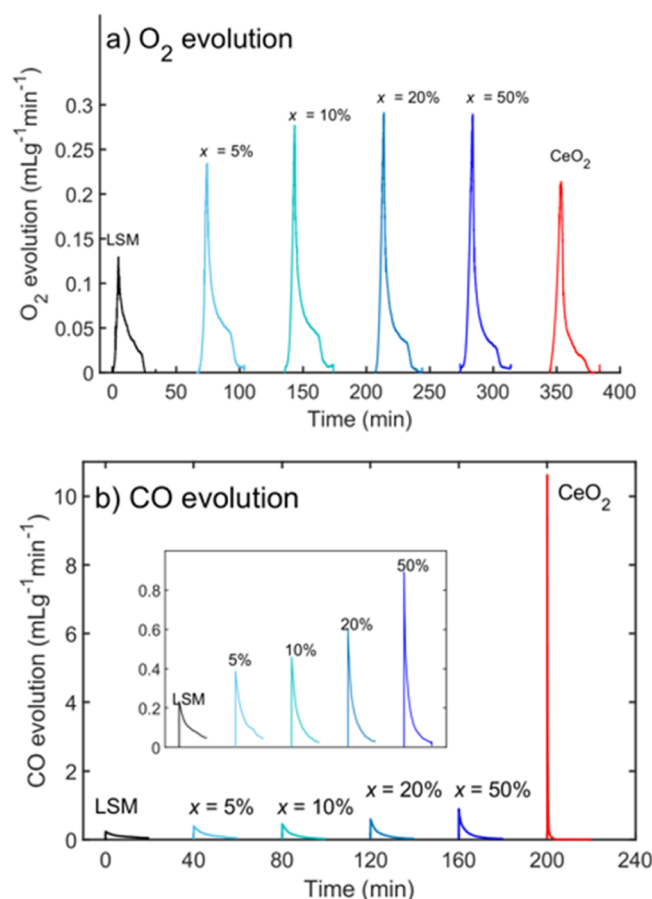
Figure 4. O_2 and CO evolution of $La_{0.65}Sr_{0.35}MnO_3-x\%CeO_2$ during a thermochemical cycle 1000−1400 °C. (a) O_2 evolution of LSM−xCeO$_2$, x = 0, 5, 10, 20, 50, and 100% for heating from 1000 to 1400 °C with a heating rate of 50 °C min^{-1}. (b) CO evolution of LSM−x%CeO$_2$, x = 0, 5, 10, 20, 50, and 100% for CO$_2$ splitting at 1400 °C. The fluorite−perovskite composite trends were zoomed in the inset for the sake of clarity.

of future solar thermochemical reactors.[15,27] For details and results of the entire temperature-screening program, including splitting in isothermal cycles and conventional two-step cycles, see Figure S2. Oxygen release of the composites during heating from 1000 to 1400 °C is presented in Figure 4a. Introducing 5 wt % of CeO$_2$ in the dual-phase composite improves the O$_2$ peak evolution by 92% to a value of 0.24 mL g^{-1} min^{-1} compared to LSM. The dual-phase composites display further synergetic oxygen release kinetics for increased CeO$_2$ content, reaching a maximum among the tested materials of 0.31 mL g^{-1} min^{-1} O$_2$ for both LSM−20%CeO$_2$ and LSM−50%CeO$_2$ compared to a peak rate of 0.21 mL g^{-1} min^{-1} for ceria. Hence, mixing LSM and CeO$_2$ on the micron scale that remain in two distinct phases results in a remarkable increase of 45 and 100% compared to its individual constituents.

The CO evolution is plotted for all tested materials in Figure 4b for CO$_2$ splitting at 1000 °C. The maximum CO evolution rate improves gradually to 0.9 mL g^{-1} min^{-1} for x = 50 wt %, which is ca. 4-fold higher than that of LSM with a peak rate of 0.2 mL g^{-1} min^{-1}. For comparison, state-of-the-art CeO$_2$ displays a peak rate of 10.6 mL g^{-1} min^{-1} in Figure 4b. Evidently, the constituents of the composite illustrated in Figure 4 display an intimate interaction in terms of CO evolution. We note that at higher temperatures (1200 °C and

above) CO$_2$ splitting results in simultaneous production of O$_2$. This is ascribed to the thermolysis of CO$_2$ (CO$_2$ → CO + 1/2 O$_2$) which is in agreement with earlier observations[49] and discussed in detail in our previous work.[15]

To further probe the interaction between CeO$_2$ and LSM in the composite, the accumulated CO production is plotted as function of time for the same conditions for LSM−50%CeO$_2$ in Figure 5. The higher oxygen release of the composite has a
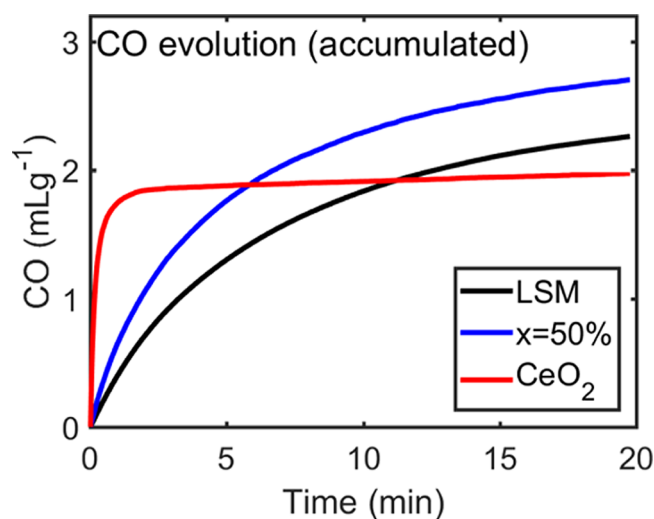

Figure 5. Cumulative CO production evolution of composite $La_{0.65}Sr_{0.35}MnO_3$−50%CeO$_2$, x = 50%, compared to the constituent phases $La_{0.65}Sr_{0.35}MnO_3$ and CeO$_2$. CO$_2$ splitting was performed at 1000 °C with a CO$_2$ concentration of 50 vol % and after reduction at 1400 °C in an Ar atmosphere.

beneficial effect on the accumulated CO evolution. For 20 min CO$_2$ splitting, the total evolved CO is 2.7 mL g^{-1} for the composite, which is 17 and 19% higher than 2.3 and 2.1 mL g^{-1} of the distinct components LSM and CeO$_2$, respectively. The total evolved CO of LSM after 20 min is lower than some values reported in the literature because these works exposed LSM to CO$_2$ for a longer time of 40 min or more.[19,27] Incomplete re-oxidation of LSM and the composite is further apparent from Figure 5, as the accumulated CO curve has not reached an asymptotic value. Employing longer exposure to CO$_2$ is expected to provide a higher accumulated yield. We did not design our experiments to maximize the CO yield but focused on the important first 20 min. For future reactor operation, shorter reaction times are relevant because it is a trade-off between the higher yield and an increased energy penalty for heating a continuous flow of the reactant gas.[27]

In summary, the interaction between the two phases has an adverse effect on the maximum fuel rate, whereas it has a synergetic effect on the peak O$_2$ evolution rate and total produced CO fuel.

3.3. Structural Analysis of Composites after Thermochemical Cycling. To study the microstructural and crystal structure evolution of the dual-phase composite after thermochemical cycling, we turn to SEM, EDS, and XRD analyses. Comparing the SEM image before and after thermochemical cycling, as shown in Figures 2e and 6a, respectively, the composites display grain growth after thermochemical cycling. Changes in the grain size are quantified by SEM image analysis are shown in Figure 6b, which show that the composite $La_{0.65}Sr_{0.35}MnO_3$−50 wt %
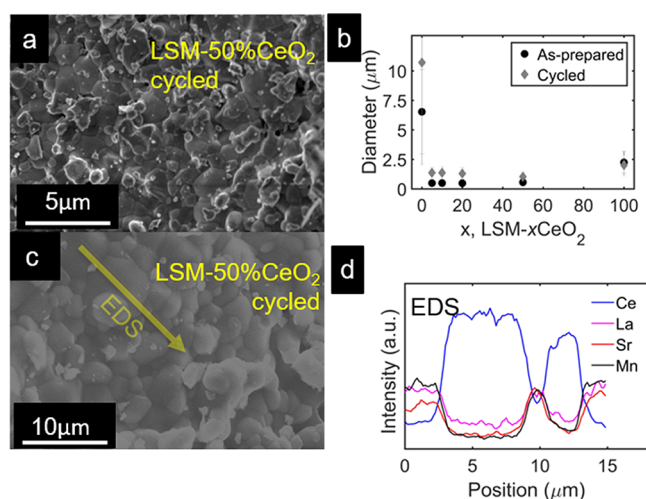
Figure 6. SEM and EDS analysis of $La_{0.5}Sr_{0.35}MnO_3-x\%CeO_2$ after thermochemical cycling. (a) Micrograph of cycled $La_{0.65}Sr_{0.35}MnO_3-50\%CeO_2$. (b) Average grain diameter for as-prepared and cycled $La_{0.65}Sr_{0.35}MnO_3-x\%CeO_2$ composites. (c) SEM picture of area used for EDS lines, shown in (d), of the thermochemically cycled LSM−50%CeO$_2$ sample.

CeO_2 changes grain size from 0.6 ± 0.2 to $1 \pm 0.4\ \mu m$, albeit, it is still smaller than ceria which displays a stable grain size before and after cycling of 2.2 ± 0.9 and $2.0 \pm 0.9\ \mu m$. One could anticipate the kinetics of the composite to decrease during thermochemical cycling because the microstructure of the cycled materials has coarsened. On the contrary, comparing Cycle 3 and Cycle 8, that is, isothermal CO_2 splitting at 1400 °C (see Supporting Information S2), there is no measurable difference in the kinetics of the fuel production peak. Lastly, distribution of metal cations captured in the EDS linescan, as shown in Figure 6d, of the composite material indicate clear and distinct CeO_2 and LSM grains. The gradient of the metal cation concentration in the grain boundary may be interpreted as interdiffusion of metal cations from each phase or a tilt of the grain boundary with respect to the electron beam.

XRD patterns of LSM−50%CeO$_2$ and that of the composite after thermochemical cycling (1000−1400 °C) as well as 20 isothermal CO_2 splitting cycles at 1400 °C are presented in Figure S2. No structural changes were observed upon the cycling of the composite material with 50 wt %CeO$_2$, on comparing Figure S3a-c. Two peaks arising at $2\theta = 26$ and 35°, as shown in Figure S3c, are ascribed to the sample powder bed made of Al_2O_3 used for holding the composites in the fixed-bed reactor, which were mixed when extracting the sample from the reactor tube. Furthermore, we probe the stability of the best performing dual-phase composite by measuring the CO evolution for 20 isothermal cycles at 1400 °C, as shown in Figure S4. Here, the peak CO evolution displays no changes over the tested cycles, which is a positive indicator for the longevity of the dual-phase composite.

Thus, SEM, EDS, and XRD after thermochemical cycling and durability test of 20 cycles collectively confirm a dual-phase composite that remains in two distinct phases with no measurable additional phases besides the fluorite and perovskite structure.

3.4. *Ex Situ* Structural Analysis of Dual-Phase Composites through Thermochemical Cycling. To gain further insights into the intimate and synergetic interaction

between the constituent phases of the composite, we investigate the structural changes upon reduction and oxidation during the thermochemical cycling experiments by *ex situ* Raman spectroscopy and powder X-ray diffraction.

Figure 7a shows the thermochemical programs applied to imitate the conditions during the thermochemical experiments,
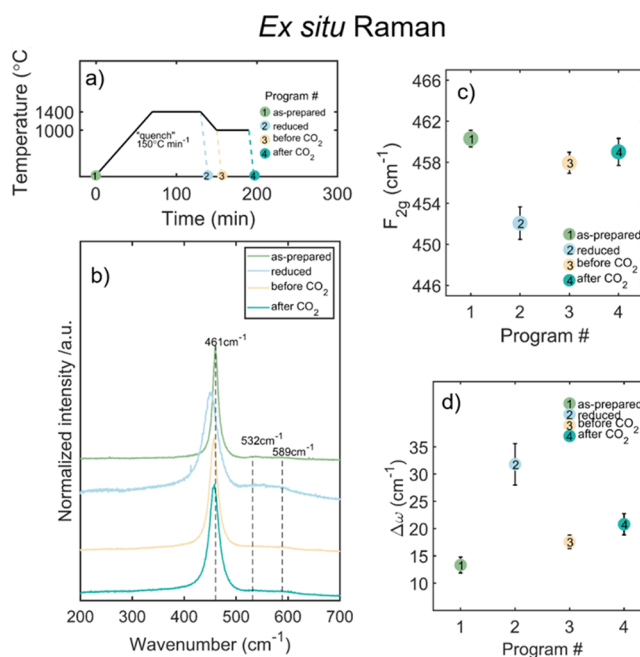

Figure 7. *Ex situ* Raman spectroscopy of composite $La_{0.65}Sr_{0.35}MnO_3-50\%CeO_2$, $x = 50$ wt %. (a) Temperature programs #1−4 employed to replicate conditions during thermochemical cycling between 1400 and 1000 °C. Dashed lines represent rapid cooling, 150 °C min^{-1}, to room temperature to "quench" near-order oxygen-cation structural changes at different stages of the cycling. (b) Raw data of samples, (c) fitted peak position, and (d) fwhm of F_{2g} mode of ceria in composite for four different thermochemical programs. (1) As-prepared, (2) reduced for 60 min at 1400 °C, (3,4) represent reduction at 1400° followed by cooling with rate of 20 °C min^{-1} to 1000 °C before and after exposure to 50 vol % CO_2 for 20 min. Error bars reflect standard deviation of the fitted parameter to Raman spectra in different spots on the same sample.

where a rapid cooling rate of 150 °C min^{-1} is utilized to "quench" the extent of reduction at important points during the thermochemical experiment for the ensuing *ex situ* Raman spectroscopy. The F_{2g} Raman peak signature for ceria of the dual-phase composite is plotted in Figure 7b, while the fitted F_{2g} peak and fwhm of the LSM−50%CeO$_2$ sample after four different temperature programs are shown in Figure 7c,d, respectively. During thermal reduction, from room temperature to 1400 °C, the peak position shifts from 461 to 452 cm^{-1}. Interestingly, there is a significant increase in wavenumber to 458 cm^{-1} in the course of cooling from 1400 to 1000 °C and a relatively smaller change to 459 cm^{-1} after exposure to CO_2 at 1000 °C. In agreement with the literature, these changes are attributed to the variation in the concentration of oxygen vacancies introduced by reduction and oxidation.[50,51] Importantly, we note that the CeO_2 phase in the composite is substantially oxidized over the course of cooling from 1400 to 1000 °C before CO_2 is introduced. To further probe this hypothesis, we turn to XRD to analyze the changes in the unit cell volume that reflects the changes in

oxygen nonstoichiometry of both phases in the dual-phase composite.

Figure 8 displays results of an *ex situ* X-ray diffraction analysis of the dual-phase composite, with the thermochemical
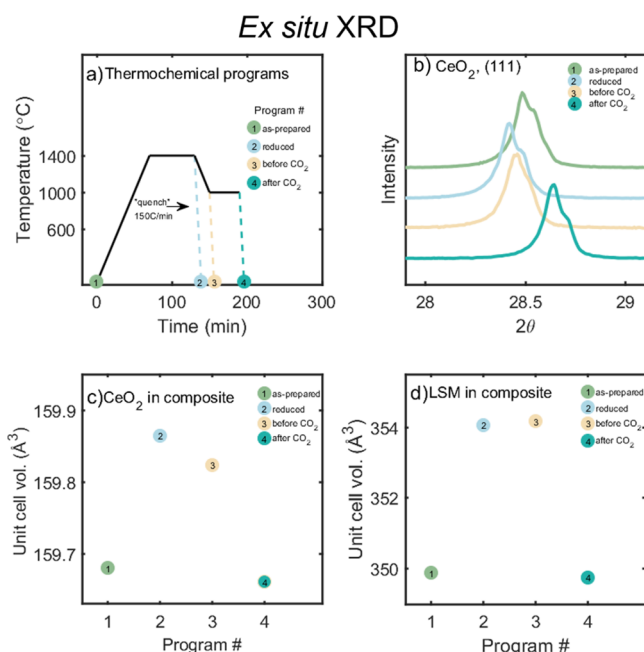
Ex situ XRD

Figure 8. Rietveld refinement results from *ex situ* XRD measurements of samples undergoing the same thermochemical program as cycling with reduction at 1400 °C and oxidation at 1000 °C. Rapid cooling (quenching) was used to maintain the reduction extent of the metal oxide at the given point of interest, Program numbers 1 to 4. (a) Thermochemical programs. (b) Narrow 2θ range of XRD showing a ceria (111) peak in the composite, (c) CeO_2 unit cell volume, and (d) unit cell volume of LSM in the composite.

programs, similar to the *ex situ* Raman study, as shown in Figure 8a. Full Rietveld refinement has been carried out for all four samples, as shown in Figures S1 and S5−S7. We exemplify the changes in the crystal structure by highlighting a narrow 2θ range to show the shift of the (111) peak of CeO_2, as shown in Figure 8b, in the dual-phase composite as a function of the program it has been exposed to. In the course of heating to 1400 °C, the peak shifts to lower angles, while a shift to higher angles is observed both during cooling and after exposure to CO_2. We quantify those changes by the determination of the unit cell volume of ceria and the LSM phase in the composite by full Rietveld refinement, as shown in Figure 8c,d, respectively. As expected, there is an inverse proportionality between the (111) peak of ceria and the unit cell volume, as shown in Figure 8b,c. An increase in the unit cell volume from 159.68 to 159.86 Å^3, that is, removal of oxygen, of ceria is reported in the course of reduction to 1400 °C, as displayed in Figure 8c and Table S1, which is in agreement with the literature.[52] For further discussions of origin of lattice expansion in CeO_2 upon reduction see Marrocchelli et al.[52] and Muhich.[53] During cooling, the unit cell volume of the ceria phase decreases, that is, due to incorporation of oxygen, to 159.82 Å^3 which is consistent with our results from Raman spectroscopy and earlier findings in spectroscopy.[46] The LSM phase also displays lattice expansion after reduction at 1400 °C, apparent by a unit cell volume increase from 349.87 to 354.05 Å^3, as shown in Figure 8d. Lattice expansion upon

introduction of O vacancies in the $LaMnO_{3-\delta}$ phase has likewise been reported in the literature.[54] Interestingly, the lattice slightly expands, indicative of oxygen removal, during cooling to 354.16 Å^3 contrary to the CeO_2 phase. After exposure to CO_2, both phases display a decrease in the unit cell volume corresponding to the oxygen uptake.

In summary, the *ex situ* analysis confirms that the introduction of oxygen vacancies in the CeO_2 and LSM result in lattice expansion of both crystal structures when tested for the solar-to-fuel conversion temperature range of 1000 to 1400 °C. Most notably, the CeO_2 phase is oxidized while cooling to 1000 °C as displayed by two independent techniques, based on bond vibrational Raman spectroscopy and XRD, whereas the perovskite phase is slightly reduced during this step of the thermochemical cycle.

3.5. Observed Synergetic Interaction of Components in the Dual-Phase Composite. Having established that dual-phase composites of the fluorite and perovskite structure display synergetic oxygen exchange under conditions relevant for solar thermochemical fuel production between 1000 and 1400 °C, we now evaluate different hypotheses to explain the observed oxygen exchange behavior.

Three mechanisms are evaluated qualitatively, based on the literature, to provide a possible mechanism for the synergetic O_2 evolution, total CO production, and the adverse low value of the maximum CO evolution rate observed for the dual-phase composites. The first explanation (i) is through doping, either Ce-doping in the LSM phase or La-doping in the ceria phase; the second (ii) is through reversible CeO_2 reduction followed by Ce^{4+} incorporation in the perovskite lattice during reduction/oxidation with the release/uptake of gaseous oxygen; the third (iii) is by ceria acting as an oxygen diffusion channel between the perovskite phase and the surrounding atmosphere.

First, we consider the literature on doping of the perovskite and ceria phase tested for solar thermochemical cycling and assess qualitatively whether doping can explain the observed trends. Jiang et al.[55] investigated the substitution of Sr by Ce on the A-site of the $La_{0.7}A_{0.3}FeO_3$ perovskite. For $La_{0.7}Ce_{0.3}FeO_3$, the maximum oxygen release rate was 10% higher, while the maximum CO evolution rate was three times higher. The authors remark a "tiny" impurity concentration of the CeO_2 phase in their synthesized perovskite, presumably due to the different ionic radii of strontium and cerium. Based on related studies of A-site substitution in perovskites, we expect that a lower content of Ce in a solid solution of $La_{0.7}Sr_{0.3-x}Ce_xFeO_3$, would have oxygen release characteristics that lie in between its endmembers $La_{0.7}Sr_{0.3}FeO_3$ and $La_{0.7}Ce_{0.3}FeO_3$.[18] In other words, a small doping concentration of cerium in the perovskite would result in a maximum oxygen release rate that is between 0 and 10% higher than $La_{0.7}Sr_{0.3}FeO_3$. In our experiment, we show that a composite with a nominal 5 wt %CeO_2 (*i.e.*, LSM−5%CeO_2) results in a 92% increase in the maximum oxygen release rate. This result is significantly higher than the 10% observed for $La_{0.7}Ce_{0.3}FeO_3$, which includes a trace amount of the CeO_2 phase. From this qualitative analysis, we reason that a small doping amount of cerium in LSM of the dual-phase composite would not be responsible for the significant increase in the maximum oxygen release rate. Furthermore, LSM−50%CeO_2 displays a 5-fold decrease in the maximum CO evolution rate compared to the weighted average which does not match with

the trend observed for the reference case of $La_{0.7}Ce_{0.3}FeO_3$ showing a higher rate.

Recently, Haeussler et al.[56] reviewed the literature on various dopants in CeO_2 and its performance for solar thermochemical cycles. According to this review, pure ceria and lanthanum-doped CeO_2 have similar performance. Specifically, Jiang et al.[57] have shown that the CO rate generation profile of $La_{0.15}Ce_{0.85}O_2$ is similar to undoped CeO_2. This result is far from the trends in our experiments considering the CO evolution curve of the LSM−50%CeO_2 composite, as shown in Figure 4b. Here, the peak CO evolution rate is 0.9 mL g^{-1} min^{-1}, which is more than 5 times lower compared to a weighted average of 5.4 mL g^{-1} min^{-1} for the two individual phases LSM and CeO_2. For the high temperatures relevant for solar thermochemical cycles, it has been established that the oxygen release profiles or thermochemical splitting profiles scale proportionally with the doping or substitution content.[18] Because our analyses show that the two phases are doped by low contents and based on the available literature we reason that the effect of doping would be too small to be the dominant mechanism for the observed trends. Instead, there must be another mechanism responsible for the significant changes observed here.

Turning to the second hypothesis (ii), where CeO_2 is reduced to metallic cerium and then being incorporated reversibly in the perovskite phase during the high-temperature step and oxidized back to the cerium oxide phase during the oxidation step. The lower peak fuel rate observed for the 50 wt % dual-phase composite, as shown in Figure 4, could be explained by Ce^{4+} ions being dissolved slowly from the perovskite phase and forming CeO_2. This change would imply that the amount of the ceria phase in the composite should decrease during reduction and increase reversibly to 50 wt % during oxidation. *Ex situ* XRD results reveal that the wt % of ceria in the composite is almost invariant to the temperature change, as shown in Table S1.

Lastly, we consider mechanism (iii) which relies on ceria functioning as an "oxygen diffusion channel" or "gateway" for lattice oxygen in the bulk of the perovskite phase to the surrounding gas phase. This description is similar to the terminology used by Huang et al.[29] and Machida et al.[34] to describe, the synergetic oxygen release in dual-phase composites of CeO_2 and $CuMnO_2$ or Fe_2O_3 tested below 1000 °C as oxygen storage materials. The low maximum peak CO rate observed during CO_2 splitting of the composite arises because ceria is oxidized (by oxygen from the perovskite) during cooling from 1400 to 1000 °C, which matches with our *ex situ* Raman spectroscopy and *ex situ* powder X-ray diffraction results. When the ceria phase is oxidized its capacity for CO production thus decreases. The oxygen change based on mechanism (iii) with preferential oxidation of the ceria phase is highlighted in Figure 9.

Preferential oxidation of ceria compared to the perovskite phase may be explained from a thermodynamic perspective considering the difference in the Gibbs free energy change oxidation of the respective metal oxides, $\Delta g_{oxidation}$. We investigate this hypothesis further, as shown in Figure 10, where it can be observed that the Gibbs free energy change of oxidation in the presence of oxygen is more negative for the CeO_2 phase compared to the perovskite phase below 1200 °C, that is, $\Delta g_{oxidation,CeO_2} < \Delta g_{oxidation,LSM}$.
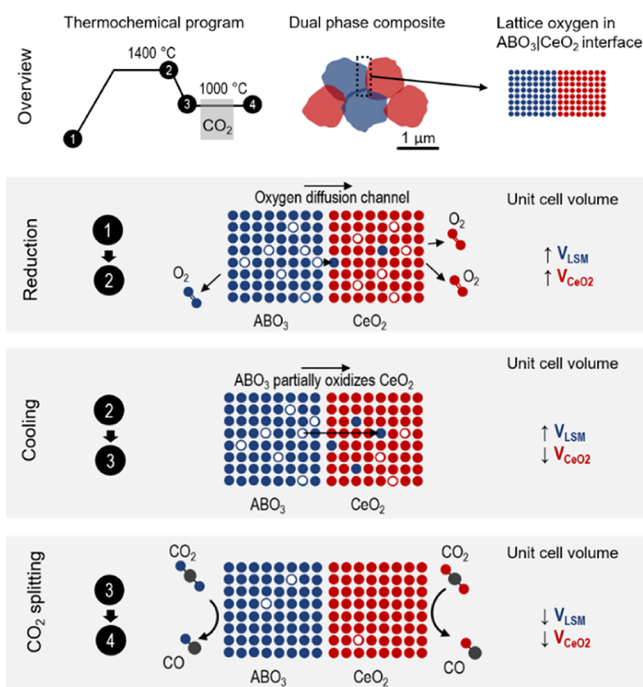

Figure 9. Interpretation of observed synergetic oxygen exchange in the dual-phase LSM−x%CeO_2 composite from *ex situ* Raman and XRD analysis. The panel "Overview" shows step 1−4 in the thermochemical programs used during the *ex situ* experiment, the composite, and an illustration of the lattice oxygen in the interface between the perovskite ABO_3 and fluorite CeO_2 structure. The panel "Reduction", "Cooling", and "CO_2 splitting" illustrates the proposed mechanism (oxygen transport from perovskite to ceria) during these three defining steps. During reduction, CeO_2 acts as an oxygen diffusion channel, promoting extra lattice oxygen to be released from the perovskite during this step. Through cooling, lattice oxygen from the perovskite oxidizes the CeO_2 phase slightly which corresponds to a decrease in unit cell volume, while the perovskite is reduced and therefore increases its volume. For the CO_2 splitting step, both the perovskite and the fluorite phase are oxidized reflected by a decrease in the unit cell volume for both phases. Because CeO_2 is already partially oxidized in the previous step, the kinetics of the CO_2 splitting reaction is more similar to that of the perovskite. We note that the proposed mechanism illustrated here is a likely one, qualitatively supported in our discussion but warrants further experimental work to prove unequivocally.

In other words, oxygen gains more energy by oxidizing ceria compared to the perovskite. This analysis indicates that, during reduction, CeO_2 may function as a fast oxygen diffusion channel that facilitates faster overall reduction of the perovskite phase, due to ceria acting as a preferential intermediate host for oxygen from the perovskite phase. However, this mechanism still warrants further experimental work.

4. CONCLUSIONS

In this work, we show enhanced oxygen exchange in the $La_{0.65}Sr_{0.35}MnO_3$−$xCeO_2$ composite system for solar thermochemical cycling compared to pure ceria and the pure perovskite. The dual-phase composites were successfully fabricated *via* co-sintering, evident by two distinct phases mixed at the micron scale. This is the first work testing the oxygen exchange for solar thermochemical fuel production using a dual-phase composite based on nonvolatile nonstoichiometric metal oxides, compared to earlier composites relying on volatile or nonvolatile stoichiometric metal oxides.
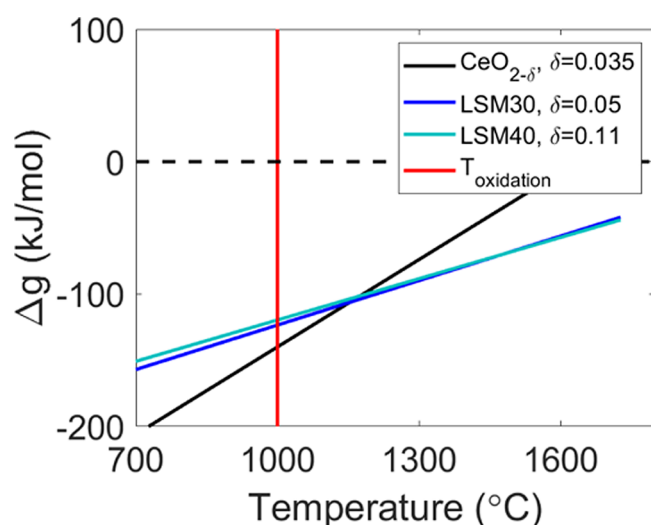
Figure 10. Gibbs free energy change of oxidation, $\Delta g_{oxidation}$ is given for the reaction $M_xO_{y-\delta} + \delta/2 O_2 \rightarrow M_xO_y$ for the metal oxides: CeO_2, $La_{0.7}Sr_{0.3}MnO_3$ and $La_{0.6}Sr_{0.4}MnO_3$. The $\Delta g_{oxidation}$ depends on the oxygen nonstoichiometries, δ: here, it is shown for the reduction extent, δ, that is reached after reduction at 1400 °C and $pO_2 = 10^{-5}$ atm extracted from Takacs et al.[2] and Bork et al.[21] The red vertical line corresponds to an oxidation temperature T_{ox} = 1000 °C.

With the $La_{0.65}Sr_{0.35}MnO_3$−50%CeO_2 dual-phase composite, we report a synergistic effect for the solar-to-fuel process in terms of higher oxygen release and higher CO conversion yield in the syngas production. Conversely, the fast oxygen exchange had an adverse effect on the peak CO evolution rate for solar-to-fuel production. The peak O_2 evolution rate is 0.31 mL g^{-1} min^{-1} in the course of heating to 1400 °C for the $La_{0.65}Sr_{0.35}MnO_3$−50%CeO_2 dual-phase oxide, which is 45 and 100% higher than CeO_2 and LSM, respectively.

Structural analyses by XRD, Raman spectroscopy, SEM, and EDS confirm a dual-phase composite that remains in two distinctive phases during thermochemical cycling. We report that there is an indication of minor cation interdiffusion leading to a small doping concentration of less than 5 mol % of La in the ceria phase after processing. *Ex situ* Raman and XRD analyses provide understanding to the synergistic oxygen exchange *via* a qualitative determination of the extent of reduction at relevant stages during thermochemical cycling. During the cooling step, that is, from 1400 to 1000 °C, it is shown that the perovskite phase is reduced, while ceria oxidizes. A likely mechanism to explain this behavior is the transport of oxygen from the perovskite to ceria. This effect can be explained further from a thermodynamics perspective, showing that the oxidation of ceria is thermodynamically favorable over the oxidation of the perovskite phase. A similar argument applies to the reduction step, where ceria can facilitate fast reduction of the perovskite phase. Thus, we describe how ceria can act as a "gateway" or "oxygen diffusion channel" for fast oxygen exchange from the perovskite acting as an oxygen reservoir at temperatures above 1000 °C. This observation, however, warrants more work to probe and prove the underlying mechanism.

The solar-to-fuel technology is facing a tremendous challenge in finding optimized materials that enhance the kinetics and increase the oxygen exchange capacity to improve the overall cycle efficiency. Dual-phase composites based on perovskites and cerium dioxide define a new strategy to

undertake that challenge and are feasible for processing *via* co-sintering. This work is the proof of concept for the solar-to-fuel technology using ceria to enable a higher and faster utilization of the large oxygen exchange capacity of a perovskite model material $La_{0.65}Sr_{0.35}MnO_3$. Owing to the ability of perovskites to host a wide variety of different elements in the crystal structure, it is possible to design perovskite materials that are even more efficient in combination with ceria. This potential should promote further studies to explore the underlying mechanism for the observed synergy in detail.

■ ASSOCIATED CONTENT

ⓢ Supporting Information

The Supporting Information is available free of charge at https://pubs.acs.org/doi/10.1021/acsami.0c04276.

Description of fixed-bed reactor setup, Rietveld refinement fits, thermochemical program with O_2 and CO evolution profiles for all tested materials, that is, $La_{0.65}Sr_{0.35}MnO_3$−x%CeO_2, x = 0, 5, 10, 20, 50, 100, XRD patterns of $La_{0.65}Sr_{0.35}MnO_3$−50%CeO_2 as-prepared, cycled and after 20 cycles, thermochemical durability test, and table of lattice volume and LSM wt % determined by Rietveld refinement (PDF)

■ AUTHOR INFORMATION

Corresponding Authors

Bilge Yildiz − *Laboratory for Electrochemical Interfaces, Department of Materials Science & Engineering and Laboratory for Electrochemical Interfaces, Department of Nuclear Science and Engineering, Massachusetts Institute of Technology, Cambridge, Massachusetts 02139, United States;* ⓞ orcid.org/0000-0002-2688-5666; Email: byildiz@mit.edu

Jennifer L. M. Rupp − *Electrochemical Materials Laboratory, Department of Materials Science and Engineering and Electrochemical Materials Laboratory, Department of Electrical Engineering and Computer Science, Massachusetts Institute of Technology, Cambridge, Massachusetts 02139, United States;* ⓞ orcid.org/0000-0001-7160-0108; Email: jrupp@mit.edu

Authors

Alexander H. Bork − *Electrochemical Materials Laboratory, Department of Materials Science and Engineering and Laboratory for Electrochemical Interfaces, Department of Materials Science & Engineering, Massachusetts Institute of Technology, Cambridge, Massachusetts 02139, United States;* ⓞ orcid.org/0000-0003-4513-9682

Alfonso J. Carrillo − *Electrochemical Materials Laboratory, Department of Materials Science and Engineering, Massachusetts Institute of Technology, Cambridge, Massachusetts 02139, United States;* ⓞ orcid.org/0000-0002-5576-9277

Zachary D. Hood − *Electrochemical Materials Laboratory, Department of Materials Science and Engineering, Massachusetts Institute of Technology, Cambridge, Massachusetts 02139, United States;* ⓞ orcid.org/0000-0002-5720-4392

Complete contact information is available at:
https://pubs.acs.org/10.1021/acsami.0c04276

■ **REFERENCES**

(1) Chueh, W. C.; Falter, C.; Abbott, M.; Scipio, D.; Furler, P.; Haile, S. M.; Steinfeld, A. High-Flux Solar-Driven Thermochemical Dissociation of CO_2 and H_2O Using Nonstoichiometric Ceria. *Science* **2010**, *330*, 1797−1801.

(2) Takacs, M.; Scheffe, J. R.; Steinfeld, A. Oxygen Non-stoichiometry and Thermodynamic Characterization of Zr Doped Ceria in the 1573−1773 K Temperature Range. *Phys. Chem. Chem. Phys.* **2015**, *17*, 7813−7822.

(3) Panlener, R. J.; Blumenthal, R. N.; Garnier, J. E. A Thermodynamic Study of Nonstoichiometric Cerium Dioxide. *J. Phys. Chem. Solids* **1975**, *36*, 1213−1222.

(4) Ackermann, S.; Sauvin, L.; Castiglioni, R.; Rupp, J. L. M.; Scheffe, J. R.; Steinfeld, A. Kinetics of CO_2 Reduction over Nonstoichiometric Ceria. *J. Phys. Chem. C* **2015**, *119*, 16452−16461.

(5) Zhao, Z.; Uddi, M.; Tsvetkov, N.; Yildiz, B.; Ghoniem, A. F. Enhanced Intermediate-Temperature CO_2 Splitting Using Non-stoichiometric Ceria and Ceria−Zirconia. *Phys. Chem. Chem. Phys.* **2017**, *19*, 25774−25785.

(6) Marxer, D.; Furler, P.; Takacs, M.; Steinfeld, A. Solar Thermochemical Splitting of Co_2 into Separate Streams of CO and O_2 with High Selectivity, Stability, Conversion, and Efficiency. *Energy Environ. Sci.* **2017**, *10*, 1142−1149.

(7) Marxer, D.; Furler, P.; Scheffe, J.; Geerlings, H.; Falter, C.; Batteiger, V.; Sizmann, A.; Steinfeld, A. Demonstration of the Entire Production Chain to Renewable Kerosene Via Solar Thermochemical Splitting of H_2O and CO_2. *Energy Fuels* **2015**, *29*, 3241−3250.

(8) Scheffe, J. R.; Steinfeld, A. Thermodynamic Analysis of Cerium-Based Oxides for Solar Thermochemical Fuel Production. *Energy Fuels* **2012**, *26*, 1928−1936.

(9) Demont, A.; Abanades, S.; Beche, E. Investigation of Perovskite Structures as Oxygen-Exchange Redox Materials for Hydrogen Production from Thermochemical Two-Step Water-Splitting Cycles. *J. Phys. Chem. C* **2014**, *118*, 12682−12692.

(10) Fu, M.; Wang, L.; Ma, T.; Ma, H.; Xu, H.; Li, X. Mechanism of CO Production around Oxygen Vacancy of $LaMnO_3$: An Efficient and Rapid Evaluation of the Doping Effect on the Kinetics and Thermodynamic Driving Force of Co_2-Splitting. *J. Mater. Chem. A* **2020**, *8*, 1709−1716.

(11) Azcondo, M. T.; Orfila, M.; Marugán, J.; Sanz, R.; Muñoz-Noval, A.; Salas-Colera, E.; Ritter, C.; García-Alvarado, F.; Amador, U. Novel Perovskite Materials for Thermal Water Splitting at Moderate Temperature. *ChemSusChem* **2019**, *12*, 4029−4037.

(12) Scheffe, J. R.; Weibel, D.; Steinfeld, A. Lanthanum−Strontium−Manganese Perovskites as Redox Materials for Solar Thermochemical Splitting of H_2O and CO_2. *Energy Fuels* **2013**, *27*, 4250−4257.

(13) Dey, S.; Naidu, B. S.; Govindaraj, A.; Rao, C. N. R. Noteworthy Performance of $La_{1−x}ca_xmno_3$ Perovskites in Generating H_2 and CO by the Thermochemical Splitting of H_2O and CO_2. *Phys. Chem. Chem. Phys.* **2015**, *17*, 122−125.

(14) Bork, A. H.; Kubicek, M.; Struzik, M.; Rupp, J. L. M. Perovskite $La_{0.6}Sr_{0.4}Cr_{1−X}Co_xO_{3−\delta}$ Solid Solutions for Solar-Thermochemical Fuel Production: Strategies to Lower the Operation Temperature. *J. Mater. Chem. A* **2015**, *3*, 15546−15557.

(15) Carrillo, A. J.; Bork, A. H.; Moser, T.; Sediva, E.; Hood, Z. D.; Rupp, J. L. M. Modifying $La_{0.6}Sr_{0.4}Mno_3$ Perovskites with Cr Incorporation for Fast Isothermal CO_2-Splitting Kinetics in Solar-Driven Thermochemical Cycles. *Adv. Energy Mater.* **2019**, *9*, 1803886.

(16) Barcellos, D. R.; Sanders, M. D.; Tong, J.; McDaniel, A. H.; O'Hayre, R. P. $BaCe_{0.25}Mn_{0.75}O_{3−\delta}$ - A Promising Perovskite-Type Oxide for Solar Thermochemical Hydrogen Production. *Energy Environ. Sci.* **2018**, *11*, 3256−3265.

(17) Cooper, T.; Scheffe, J. R.; Galvez, M. E.; Jacot, R.; Patzke, G.; Steinfeld, A. Lanthanum Manganite Perovskites with Ca/Sr A-Site and Al B-Site Doping as Effective Oxygen Exchange Materials for Solar Thermochemical Fuel Production. *Energy.Technol.* **2015**, *3*, 1130−1142.

(18) Kubicek, M.; Bork, A. H.; Rupp, J. L. M. Perovskite Oxides−a Review on a Versatile Material Class for Solar-to-Fuel Conversion Processes. *J. Mater. Chem. A* **2017**, *5*, 11983.

(19) Yang, C.-K.; Yamazaki, Y.; Aydin, A.; Haile, S. M. Thermodynamic and Kinetic Assessments of Strontium-Doped Lanthanum Manganite Perovskites for Two-Step Thermochemical Water Splitting. *J. Mater. Chem. A* **2014**, *2*, 13612−13623.

(20) McDaniel, A. H.; Miller, E. C.; Arifin, D.; Ambrosini, A.; Coker, E. N.; O'Hayre, R.; Chueh, W. C.; Tong, J. Sr-and Mn-Doped $LaAlO_{3−\delta}$ for Solar Thermochemical H_2 and CO Production. *Energy Environ. Sci.* **2013**, *6*, 2424−2428.

(21) Bork, A. H.; Povoden-Karadeniz, E.; Rupp, J. L. M. Modeling Thermochemical Solar-to-Fuel Conversion: Calphad for Thermodynamic Assessment Studies of Perovskites, Exemplified for (La, Sr)MnO_3. *Adv. Energy Mater.* **2017**, *7*, 1601086.

(22) Bork, A. H.; Povoden-Karadeniz, E.; Carrillo, A. J.; Rupp, J. L. M. Thermodynamic Assessment of the Solar-to-Fuel Performance of $La_{0.6}Sr_{0.4}Mn_{1−y}Cr_yO_{3−\delta}$ Perovskite Solid Solution Series. *Acta Mater.* **2019**, *178*, 163−172.

(23) Kim, Y.; Jeong, S. J.; Koo, B.; Lee, S.; Kwak, N. W.; Jung, W. Study of the Surface Reaction Kinetics of (La, Sr)$MnO_{3−\delta}$ Oxygen Carriers for Solar Thermochemical Fuel Production. *J. Mater. Chem. A* **2018**, *6*, 13082−13089.

(24) Jouannaux, J.; Haeussler, A.; Drobek, M.; Ayral, A.; Abanades, S.; Julbe, A. Lanthanum Manganite Perovskite Ceramic Powders for CO_2 Splitting: Influence of Pechini Synthesis Parameters on Sinterability and Reactivity. *Ceram. Int.* **2019**, *45*, 15636−15648.

(25) Dey, S.; Naidu, B. S.; Rao, C. N. R. Beneficial Effects of Substituting Trivalent Ions in the B-Site of $La_{0.5}Sr_{0.5}Mn_{1−x}A_xO_3$ (A= Al, Ga, Sc) on the Thermochemical Generation of CO and H_2 from CO_2 and H_2O. *Dalton Trans.* **2016**, *45*, 2430−2435.

(26) Takacs, M.; Hoes, M.; Caduff, M.; Cooper, T.; Scheffe, J. R.; Steinfeld, A. Oxygen Nonstoichiometry, Defect Equilibria, and Thermodynamic Characterization of $LaMnO_3$ Perovskites with Ca/Sr a-Site and Al B-Site Doping. *Acta Mater.* **2016**, *103*, 700−710.

(27) Ignatowich, M. J.; Bork, A. H.; Davenport, T. C.; Rupp, J. L. M.; Yang, C.-K.; Yamazaki, Y.; Haile, S. M. Thermo-Kinetic Limitation in Fuel Production Rates from $La_{1-x}Sr_xMnO_{3−\delta}$ in Thermochemical Cycling. *MRS Commun.* **2017**, *7*, 873−878.

(28) Zhai, S.; Rojas, J.; Ahlborg, N.; Lim, K.; Toney, M. F.; Jin, H.; Chueh, W. C.; Majumdar, A. The Use of Poly-Cation Oxides to Lower the Temperature of Two-Step Thermochemical Water Splitting. *Energy Environ. Sci.* **2018**, *11*, 2172−2178.

(29) Huang, X.; Ni, C.; Zhao, G.; Irvine, J. T. S. Oxygen Storage Capacity and Thermal Stability of the $CuMnO_2$−CeO_2 Composite System. *J. Mater. Chem. A* **2015**, *3*, 12958−12964.

(30) Otsuka, K.; Wang, Y.; Nakamura, M. Direct Conversion of Methane to Synthesis Gas Through Gas−Solid Reaction Using CeO_2−ZrO_2 Solid Solution at Moderate Temperature. *Appl. Catal., A* **1999**, *183*, 317−324.

(31) Trovarelli, A.; de Leitenburg, C.; Boaro, M.; Dolcetti, G. The Utilization of Ceria in Industrial Catalysis. *Catal. Today* **1999**, *50*, 353−367.

(32) Machida, M.; Ueno, M.; Omura, T.; Kurusu, S.; Hinokuma, S.; Nanba, T.; Shinozaki, O.; Furutani, H. CeO_2-Grafted Mn−Fe Oxide Composites as Alternative Oxygen-Storage Materials for Three-Way Catalysts: Laboratory and Chassis Dynamometer Tests. *Ind. Eng. Chem. Res.* **2017**, *56*, 3184−3193.

(33) Zhang, D.; Kawada, T.; Yoshioka, F.; Machida, M. Oxygen Gateway Effect of $CeO_2/La_2O_2SO_4$ Composite Oxygen Storage Materials. *ACS Omega* **2016**, *1*, 789−798.

(34) Machida, M.; Kawada, T.; Fujii, H.; Hinokuma, S. The Role of CeO_2 as a Gateway for Oxygen Storage over CeO_2-Grafted Fe_2O_3 Composite Materials. *J. Phys. Chem. C* **2015**, *119*, 24932−24941.

(35) Scheffe, J. R.; Li, J.; Weimer, A. W. A Spinel Ferrite/Hercynite Water-Splitting Redox Cycle. *Int. J. Hydrogen Energy* **2010**, *35*, 3333−3340.

(36) Scheffe, J. R.; Steinfeld, A. Oxygen Exchange Materials for Solar Thermochemical Splitting of H_2O and CO_2: A Review. *Mater. Today* **2014**, *17*, 341−348.

(37) Mogensen, M.; Sammes, N. M.; Tompsett, G. A. Physical, Chemical and Electrochemical Properties of Pure and Doped Ceria. *Solid State Ionics* **2000**, *129*, 63−94.

(38) Dey, S.; Rao, C. N. R. Splitting of Co_2 by Manganite Perovskites to Generate CO by Solar Isothermal Redox Cycling. *ACS Energy Lett.* **2016**, *1*, 237−243.

(39) Cutler, R. A.; Meixner, D. L. Ceria−Lanthanum Strontium Manganite Composites for Use in Oxygen Generation Systems. *Solid State Ionics* **2003**, *159*, 9−19.

(40) Mitchell, J. F.; Argyriou, D.; Potter, C.; Hinks, D.; Jorgensen, J.; Bader, S. Structural Phase Diagram of $La_{1−x}Sr_xMnO_{3+\delta}$: Relationship to Magnetic and Transport Properties. *Phys. Rev. B* **1996**, *54*, 6172.

(41) Sediva, E.; Defferriere, T.; Perry, N. H.; Tuller, H. L.; Rupp, J. L. M. In Situ Method Correlating Raman Vibrational Characteristics to Chemical Expansion Via Oxygen Nonstoichiometry of Perovskite Thin Films. *Adv. Mater.* **2019**, *31*, 1902493.

(42) Rupp, J. L. M.; Fabbri, E.; Marrocchelli, D.; Han, J.-W.; Chen, D.; Traversa, E.; Tuller, H. L.; Yildiz, B. Scalable Oxygen-Ion Transport Kinetics in Metal-Oxide Films: Impact of Thermally Induced Lattice Compaction in Acceptor Doped Ceria Films. *Adv. Funct. Mater.* **2014**, *24*, 1562−1574.

(43) Shi, Y.; Bork, A. H.; Schweiger, S.; Rupp, J. L. M. The Effect of Mechanical Twisting on Oxygen Ionic Transport in Solid-State Energy Conversion Membranes. *Nat. Mater.* **2015**, *14*, 721.

(44) McBride, J. R.; Hass, K. C.; Poindexter, B. D.; Weber, W. H. Raman and X-Ray Studies of $Ce_{1−x}RE_xO_{2−y}$, Where RE= La, Pr, Nd, Eu, Gd, and Tb. *J. Appl. Phys.* **1994**, *76*, 2435−2441.

(45) Gulyaev, R. V.; Kardash, T. Y.; Malykhin, S. E.; Stonkus, O. A.; Ivanova, A. S.; Boronin, A. I. The Local Structure of $Pd_xCe_{1−x}O_{2−x−\delta}$ Solid Solutions. *Phys. Chem. Chem. Phys.* **2014**, *16*, 13523−13539.

(46) Schmitt, R.; Nenning, A.; Kraynis, O.; Korobko, R.; Frenkel, A. I.; Lubomirsky, I.; Haile, S. M.; Rupp, J. L. M. A Review of Defect Structure and Chemistry in Ceria and Its Solid Solutions. *Chem. Soc. Rev.* **2020**, *49*, 554−592.

(47) Mandal, S.; Santra, C.; Bando, K. K.; James, O. O.; Maity, S.; Mehta, D.; Chowdhury, B. Aerobic Oxidation of Benzyl Alcohol over Mesoporous Mn-Doped Ceria Supported Au Nanoparticle Catalyst. *J. Mol. Catal. A: Chem.* **2013**, *378*, 47−56.

(48) Schmitt, R.; Spring, J.; Korobko, R.; Rupp, J. L. M. Design of Oxygen Vacancy Configuration for Memristive Systems. *ACS Nano* **2017**, *11*, 8881−8891.

(49) Jiang, Q.; Chen, Z.; Tong, J.; Yang, M.; Jiang, Z.; Li, C. Direct Thermolysis of CO_2 into CO and O_2. *Chem. Commun.* **2017**, *53*, 1188−1191.

(50) Acharya, S. A.; Gaikwad, V. M.; Sathe, V.; Kulkarni, S. K. Influence of Gadolinium Doping on the Structure and Defects of Ceria under Fuel Cell Operating Temperature. *Appl. Phys. Lett.* **2014**, *104*, 113508.

(51) Dohčević-Mitrović, Z.; Popović, Z.; Šćepanović, M. Anharmonicity Effects in Nanocrystals Studied by Raman Scattering Spectroscopy. *Acta Physica Polonica-Series A General Physics* **2009**, *116*, 36.

(52) Marrocchelli, D.; Bishop, S. R.; Tuller, H. L.; Yildiz, B. Understanding Chemical Expansion in Non-Stoichiometric Oxides: Ceria and Zirconia Case Studies. *Adv. Funct. Mater.* **2012**, *22*, 1958−1965.

(53) Muhich, C. L. Re-Evaluating CeO_2 Expansion Upon Reduction: Noncounterpoised Forces, Not Ionic Radius Effects, Are the Cause. *J. Phys. Chem. C* **2017**, *121*, 8052−8059.

(54) Töpfer, J.; Goodenough, J. B. $LaMnO_{3+\delta}$ Revisited. *J. Solid State Chem.* **1997**, *130*, 117−128.

(55) Jiang, Q.; Tong, J.; Zhou, G.; Jiang, Z.; Li, Z.; Li, C. Thermochemical CO_2 Splitting Reaction with Supported $La_xA_{1−x}Fe_yB_{1−y}O_3$ (A= Sr, Ce, B= Co, Mn; 0 x, y 1) Perovskite Oxides. *Sol. Energy* **2014**, *103*, 425−437.

(56) Haeussler, A.; Abanades, S.; Abanades, S.; Jouannaux, J.; Drobek, M.; Ayral, A.; Julbe, A. Recent Progress on Ceria Doping and Shaping Strategies for Solar Thermochemical Water and CO_2 Splitting Cycles. *AIMS Mater. Sci.* **2019**, *6*, 657.

(57) Jiang, Q.; Zhou, G.; Jiang, Z.; Li, C. Thermochemical CO_2 Splitting Reaction with $Ce_xM_{1−x}O_{2−\delta}$ (M= Ti^{4+}, Sn^{4+}, Hf^{4+}, Zr^{4+}, La^{3+}, Y^{3+} and Sm^{3+}) Solid Solutions. *Sol. Energy* **2014**, *99*, 55−66.